J Mater Sci: Mater Electron (2021) 32:9675–9684

Effect of sintering temperature on structural, dielectric, and electrical property studies of $Bi_4NdTi_3FeO_{15}$ aurivillius ceramics

J. Praveen Kumar[1], K. S. K. R. Chandra Sekhar[2], T. Durga Rao[3], P. D. Babu[4], and Patri Tirupathi[1,*]

[1] Department of Physics, Rajiv Gandhi University of Knowledge Technologies (AP-IIIT), RK Valley, Kadapa 516330, India
[2] Department of Engineering Physics, Andhra University College of Engineering, Visakhapatam 530003, India
[3] Department of Physics, Institute of Science, GITAM (Deemed To Be University), Visakhapatnam, Andhra Pradesh 530045, India
[4] UGC-DAE Consortium for Scientific Research, Mumbai Center, BARC, Mumbai 400085, India

Received: 12 November 2020
Accepted: 23 February 2021
Published online: 11 March 2021

ABSTRACT

The effect of sintering temperature on the structural, magnetic, dielectric, and electric properties of four-layered $Bi_4NdTi_3FeO_{15}$ Aurivillius multiferroic ceramics was studied. The ceramics was prepared by conventional solid-state reaction. The Rietveld refined room temperature (RT) X-ray diffraction and Raman studies revealed that the samples exhibited an orthorhombic structure with $A2_1am$ space group. The surface morphology studies indicated that the samples exhibited non-uniform and randomly oriented plate-like grains. The *P*–*E* hysteresis loops of the samples showed an unsaturated polarization even at a high field of 90 kV/cm, indicates weak ferroelectric at RT. Room temperature magnetization curves indicate weak antiferromagnetic nature with remanent magnetization ~ 4 memu/g. The *M*–*H* loops at low temperature 10 K showed the ferromagnetic nature. The temperature dependence of dielectric and impedance data showed a dielectric relaxation which could be ascribed to short-range movements of oxygen vacancies.

1 Introduction

Multiferroic materials have been the surge of interest for several decades owing to the coexistence of more than one ferroic order in the same phase. These materials have potential for device applications such as memory devices, spintronics, sensors [1]. In recent years, the study of perovskite layered bismuth-based Aurivillius phase materials, with the general chemical formula of $(Bi_2O_2)^{2+}$ $(A_{n-1}B_nO_{3n+1})^{2-}$ (*A* = Na, Sr, Bi, etc., *B* = Ti, Nb, etc.), has been an active area of research due to their excellent dielectric, ferroelectric, and optical properties [2, 3]. Herein, the bismuth-based Aurivillius family with perovskite, $(A_{n-1}B_nO_{3n+1})^{2-}$ layers are interlayered between the fluorite-like layers $(Bi_2O_2)^{2+}$, where *n* is the layer number

Address correspondence to E-mail: ptirupathi36@gmail.com

https://doi.org/10.1007/s10854-021-05628-9

of the perovskite-like layers [3–5]. Among the reported Aurivillius compounds, Bi_3TiNbO_9 (n = 2) and $Bi_4Ti_3O_{12}$ (n = 3) have been well studied for their excellent dielectric and ferroelectric properties along with very low fatigue [6, 7]. Furthermore, the researchers are motivated to investigate the multiferroic properties of $Bi_4Ti_3O_{12}$ (n = 3) with the substitution of elements at Ti-site [8, 9]. However, low magnetic moment and lack of long-range magnetic ordering are observed in Fe^{3+} doped $Bi_4Ti_3O_{12}$ samples at the Ti site [9, 10].

Remarkable work on a four-layered (n = 4) bismuth-based Aurivillius $Bi_5Ti_4O_{15}$ (BFTO) compound has been carried out to tune their multiferroic property by cation engineering. Further, BFTO is known to be a good single-phase multiferroic with high ferroelectric Curie temperature (Tc = 750 °C). It shows a structural phase transition from $A2_1am$ to the $I4/mmm$ space group. For the first time, a typical four-layered $Bi_5Ti_3FeO_{15}$ (BTFO) was blended by inserting 1 mol $BiFeO_3$ into1 mol $Bi_4Ti_3O_{12}$, and the magnetic behavior of BFTO is determined to be antiferromagnetic (AFM) order. Mao et al. modified the magnetic behavior from AFM to ferromagnetic (FM) state by introducing half amount of Co ions at Fe sites in BFTO [10, 11]. Later, the regulation of magnetic behavior has been investigated widely by doping magnetic ions Fe/ Cr/ Mn, and Ni at Fe or Ti sites in several Aurivillius compounds with different layer number n [11–15].

On the other hand, a large number of imperfections are often observed at Bi site (A-site) in BFTO Aurivillius layer compound series with n = 4 due to the volatilization Bi-atom well above 850 °C. The high-temperature sintering normally leads to Bi-vacancies which leads to the creation of oxygen vacancies and hence, the compositional inhomogeneities occur in the material. Further, a random distribution of Ti and Fe metal ions at B-sites is inevitable in BFTO ceramic [16–21]. In general, the d^0-state of A-site cation as well as the presence of oxygen vacancies determine the ferroelectric and electrical properties of the materials. The ferroelectric properties could be tailored either with d^0 at A-site ionic and reduction in oxygen vacancies.

It has been reported that substitution of rare-earth ions at Bi-site is reported to improve the ferroelectric properties by suppressing the oxygen vacancies in Bi-based compounds [2, 22]. Further, the doping of Ti-site by Nb^{5+}, V^{5+}, W^{6+}, ions suppresses the concentration of oxygen vacancies and consequently improves the insulating character [2, 13, 18]. Based on the above discussion, the co-substitution of rare earth Nd^{3+} ion at Bi-site and Fe^{3+} at Ti-site in $Bi_5Ti_4O_{15}$ Aurivillius compound, i.e., $Bi_4NdTi_3FeO_{15}$(BNFT) ceramics will have better magnetic, ferroelectric, and dielectric properties. It is also interesting to investigate the influence of sintering temperature on structural, multiferroic, and dielectric properties of BNFT ceramics. In this work, BNFT ceramics have been synthesized by using solid-state synthesis and investigated structural, magnetic, and ferroelectric polarization properties systematically with the variation of sintering temperature.

2 Experimental

The co-substitution of Nd^{3+} and Fe^{3+} ions in $Bi_4Ti_3O_{15}$, i.e., $Bi_4NdTi_3FeO_{15}$ (BNFT) four-layered Aurivillius compounds was synthesized via a conventional solid-state reaction method. The raw materials Bi_2O_3, Fe_2O_3, Nd_2O_3, and TiO_2 were added in the stoichiometric ratio and then mixed, hand-grinded in acetone medium. Further, the powders were calcinated at 830 °C, 850 °C, and 900 °C for 8 h, respectively. The pre-sintered powder was then ground again and subsequently pressed into circular pellets with 1 mm thickness and 10 mm diameter. These pellets were sintered at 900 °C, 950 °C, and 1000 °C for 5 h and entitled as BNFT-900, BNFT-950, and BNFT-1000, respectively. The phase formation of ceramics was investigated by using the powder X-ray diffraction technique with Cu-Kα-radiation. A field-emission scanning electron microscope (FE-SEM, Sirion 200, FEI Company) was used to characterize the surface morphology of the sintered pellets. Raman spectra of the ceramics were recorded in the range of 100–1000 cm^{-1} using MODEL 2018 RM by 532 nm Laser source. The polarization (P) vs electric field (E) measurements were carried by using TF-Analyzer 2000 (aixACCT systems, GmbH) on the silver-coated pellets. The magnetic measurements were carried out with SQUID magnetometer system (MPMS-Quantum Design, CA, USA). The dielectric response and impedance analysis were performed with Wayne Kerr 6500B impedance analyzer on the silver-coated sintered ceramics of thickness ~ 1–1.5 mm in the frequency and temperature range of 1 kHz to 1 MHz and 300–800 K, respectively.

3 Results and discussion

3.1 X-ray diffraction studies

Figure 1 shows the XRD patterns of all the sintered samples. The XRD patterns indicated that all the diffraction peaks are well-matched with the standard powder diffraction data [Joint Committee on Powder Diffraction Standards (JCPDS) No. 38–1257] of $Bi_4Ti_3FeO_{15}$ (BTFO) samples. The highest intensity of (119) reflection in the patterns supports that the samples belong to Aurivillius compounds with the general formula (1, 1, $2n + 1$) [23]. The samples exhibit a four-layered Aurivillius structure. No secondary phases have been detected in the XRD patterns. With variation of sintering temperature leads to the shifting of peak positions to a higher 2θ side demonstrating a decrease in lattice parameters. The shift is more in the BNFT-950 sample, indicating a large distortion a/b in the sample sintered at 950 °C. The XRD patterns are fitted with Fullprof software to analyze the crystal structure of the samples and are shown in Fig. 2a–c. The refinement reveals that all the samples are stabilized in the orthorhombic structure of with $A2_1am$ space group. The estimated lattice parameters are: $a = 5.4322 \pm 0.00085$ Å, $b = 5.4255 \pm 0.00086$ Å, $c = 41.2768 \pm 0.00334$ Å and volume $(V) = 1216.52$ $(Å)^3$ for the sample BNFT-900, $a = 5.4342 \pm 0.00032$ Å, $b = 5.4256 \pm 0.00065$ Å, $c = 41.229 \pm 0.0032$ Å and volume $(V) = 1215.59$ $(Å)^3$ for the sample BNFT-950, and $a = 5.4341 \pm 0.00012$ Å, $b = 5.4263 \pm 0.00052$ Å, $c = 41.2573 \pm 0.0012$ Å and volume $(V) = 1216.55$ $(Å)^3$for the sample BNFT-1000 respectively. The obtained values are well consistent with the previous literature [3, 13]. The lattice distortion can be quantified using a factor called orthorhombicity, which is defined as $\delta = 2\ (a\text{-}b)/(a + b)$. The orthorhombocity for BNFT-900, BNFT-950, and BNFT-1000 samples obtained is 0.00122, 0.00158, and 0.00144, respectively. The calculated orthorhombocity reveals that the distortion is maximum in the BNFT-950 sample. These observations are in accordance with recent reported rare-earth-doped Aurivillius ceramics that leads distortions in structural can tailor the magnetic, ferroelectric, and dielectric properties of the samples [3, 13, 18].

3.2 Field emission scanning electron microscopy

Field emission scanning electron micrographs of the BNFT samples sintered at three different temperatures are shown in Fig. 3a–c. The surface morphology of the sintered pellets clearly shows the formation of plate-like structures and randomly oriented non-uniform grains. The formation of the plate-like microstructure has also been reported in the literature [24] and is a typical characteristic feature of layered type Aurivillius samples. It is reported that in Aurivillius type layered samples, the a/b plane grows faster than (001) plane due to the lower surface energy of (001) plane than that of a/b plane and leads to the plate-like shape of the grains [25]. The calculated average grain size ranges from 1.5 to 2 μm for all sintered ceramics. An increase in sintering temperature leads to a decrease in porosity [15] is clearly shown inset Fig. 3a–c in magnified view. The rare earth ion(Nd^{3+}) doping influences the grain kinetics during the sintering process and suppresses the grain boundary diffusion. In cooperation with proper sintering and 4f ((Nd^{3+}) ions lead to a better

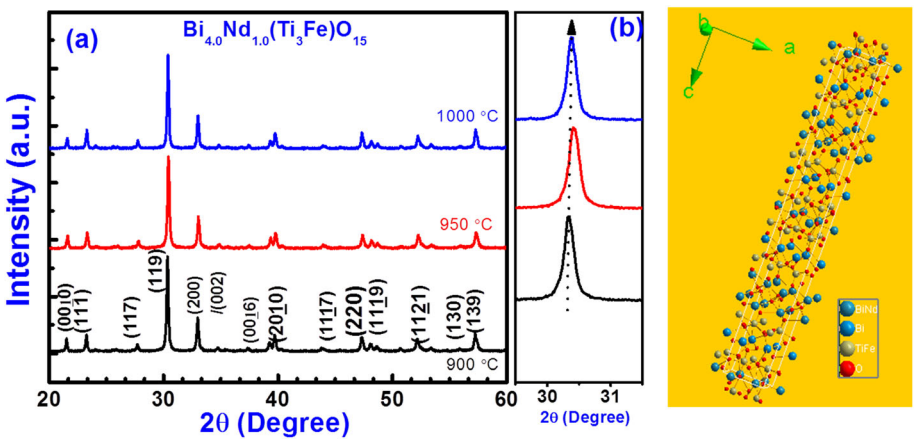

Fig. 1 X-ray diffraction pattern of $Bi_{4.0}Nd_{1.0}(Ti_3Fe)O_{15}$ sintered at various temperatures

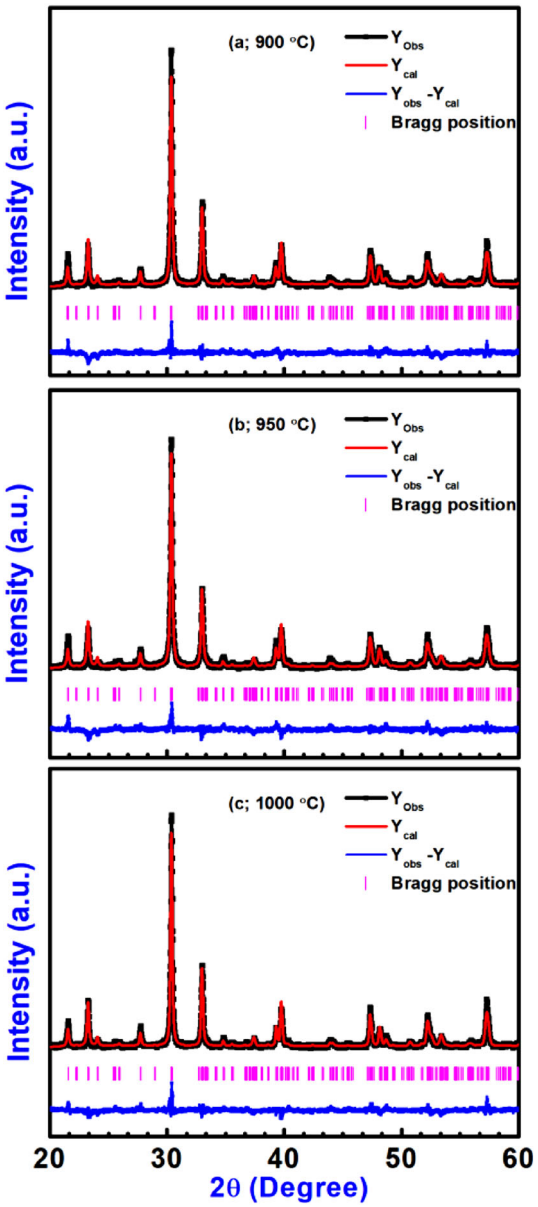

Fig. 2 **a**–**c** Rietveld X-ray diffraction pattern of $Bi_{4.0}Nd_{1.0}(Ti_3Fe)O_{15}$ ceramic sintered at three different sintered (900, 950 and 1000 °C) temperature regions

arrangement of particles and consequently to improved compactness in prepared Aurivillius ceramics [26, 27]. In addition, the densities of the ceramic pellets were calculated and are mentioned here (a) 5. 102 g/cc for 900 °C (b) 5. 31 g/cc for 950 °C (c) 5. 24 g/cc for 1000 °C, respectively. The calculated density values evident that the sintering temperature 950 °C optimal for the BNFTO Aurivillius ceramics is shown as a plot between the density v/s sintering temperature in Fig. 3d.

3.3 Raman spectroscopic studies

The Raman spectra of BNFT ceramics are shown in Fig. 4a. The measured spectra are fitted and deconvoluted to get individual modes as shown in Fig. 4b for BNFT-900, 950 and 1000 samples is shown. There are 11 noticeable Raman modes that are identified at 108, 124, 151, 219, 266, 330, 530, 566, 689, 702, 740, and 859 cm^{-1}. The low-frequency modes located at around, 108 cm^{-1}, 124 cm^{-1}, and 151 cm^{-1} designated as ν_1, ν_2, and ν_3, respectively, arise from the vibration of Bi^{3+} ions at *A*-site in perovskite-like layers. Further, the high-frequency mode observed at 266 cm^{-1} noted as ν_5 can be attributed to the torsional bending of TiO_6 vibration of the octahedral of Ti–O. Also, the doublets appear at 530 cm^{-1} and 566 cm^{-1} denoted as ν_7 and ν_8 which are originated from the peak splitting of octahedral corresponding to TiO_6 and FeO_6 octahedra, respectively. Further, two more modes ν_9 and ν_{10} noted at 702 and 740 cm^{-1} can be considered as a moment of Bi–Fe–O perovskite layer and the torsional bending of FeO_6 octahedron [28–31]. The observed mode ν_{11} at 859 cm^{-1} is due to the BO_6 octahedral stretching vibration. With sintering temperature, there have been significant changes in intensity and positions of modes in BNFT-950 and BNFT-1000 samples compared to that in BNFT-900 sample could be understood the impact of sintering temperature [30, 31].

3.4 Magnetic studies

The magnetic field dependence magnetization of samples is shown in Fig. 5. The magnetic hysteresis loop (*M*–*H*) measurements are performed at 300 K. A linear variation of magnetization with the magnetic field is observed in all the samples. Further, no significant changes in *M*–*H* loops are observed indicating the weak influence of sintering temperature on the magnetic ordering/interactions in the samples. The *M*–*H* plots show almost a linear variation of magnetization with a magnetic field. It is worth mentioning that the substitution of Nd^{3+} rare earth ion at diamagnetic Bi^{3+} ion and Fe^{3+} ion at Ti^{4+} site both effectively increases the net magnetic moment in $Bi_4NdTi_3FeO_{15}$ Aurivillius ceramics. Taking into account of the contributions of both the Nd^{3+} ions and intermediate-spin Fe^{3+}ions to the net magnetization, the total effective weak ferromagnetic M–H loops at cryogenic and room temperature is shown

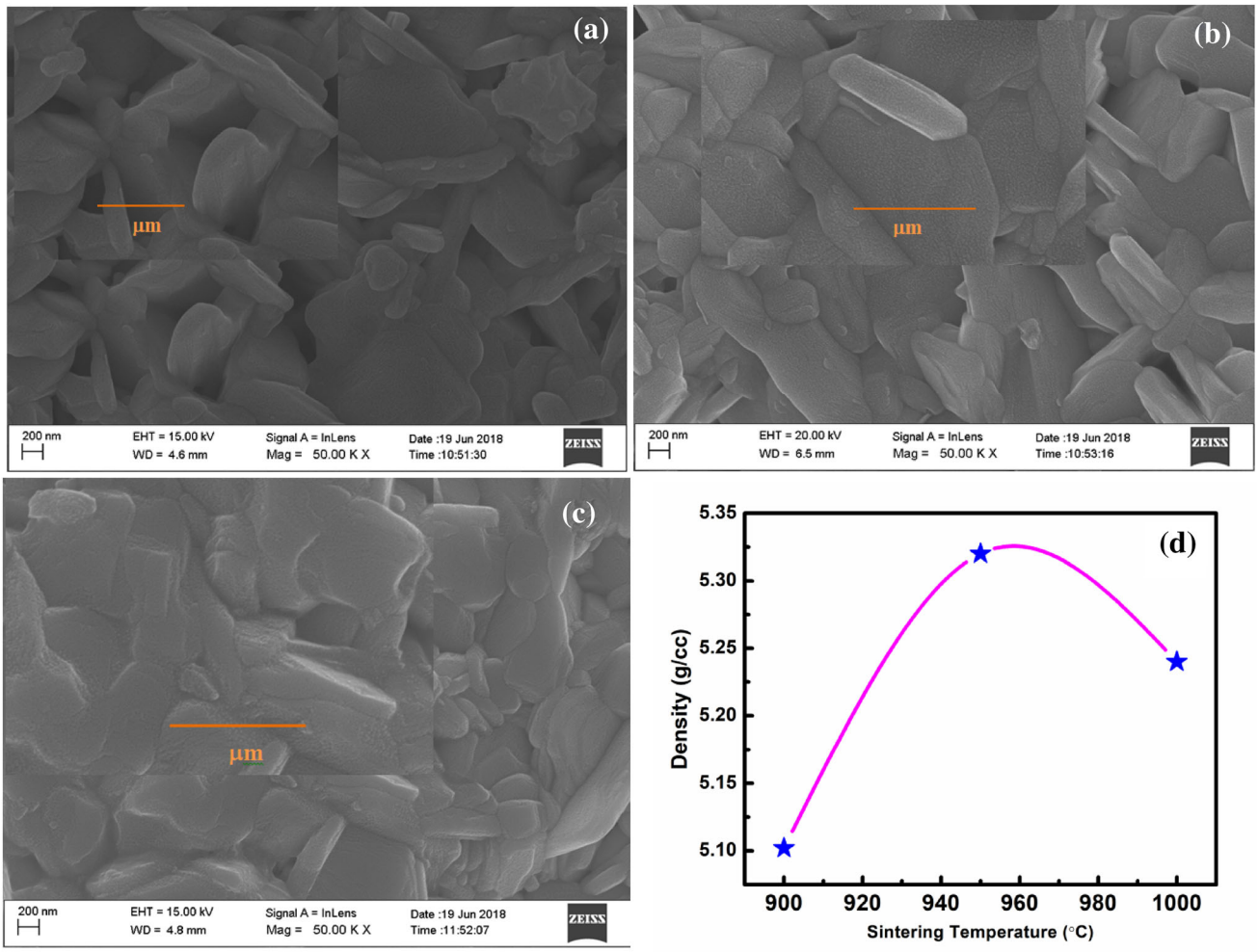

Fig. 3 FESEM images for the $Bi_{4.0}Nd_{1.0}(Ti_3Fe)\ O_{15}$ Sintered at three different temperatures 900 °C, 950 °C, and 1000 °C, respectively. Figure 3d shows the variation of density of the pellets with sintering temperature

Fig. 5. However, it has been revealed that *M*–*H* loops present small and nonzero remanent and coercive fields which is consistent with the literature [32].

The nonzero remanent magnetization could be attributed to weak ferromagnetism. The substitution of Nd^{3+} ions at Bi^{3+} sites would distort the crystal structure of the samples due to the mismatch of their ionic sizes. The distortions would change the Fe^{3+}–O^{2-}–Fe^{3+} bond angle and Fe–O bond distances and hence, affect the spin structure of the samples [31, 32]. In addition to this, the presence of mixed-valence states of Fe^{2+} and Fe^{3+}ions may develop Fe^{3+}–O^{2-}–Fe^{2+} ferromagnetic exchange interactions along with Fe^{3+}–O^{2-}–Fe^{3+} superexchange interactions and hence, the appearance of weak ferromagnetism in the samples. Further, the remanent magnetization ($2M_r$) of the samples observed in this work is nearly 4 memu/g. The higher M_r value could be attributed to the high density of the ceramics and modifications of structural parameters such as Fe–O bond lengths [8, 12]. The magnetic properties of the samples are not influenced by an increase in sintering temperature. The inset shows the nonlinear behavior of the *M*–*H* loop performed at 10 K for the BNFT-950 sample.

3.5 Ferroelectric studies

Polarization (*P*)–Electric field (E) hysteresis loops of BNFT samples are shown in Fig. 6. The saturation polarization loops have not been observed even under the applied electric field of 90 kV/cm. The loops are appeared to be of low quality which is quite usual because of the presence of high leakage currents present in these systems [33]. The leakage

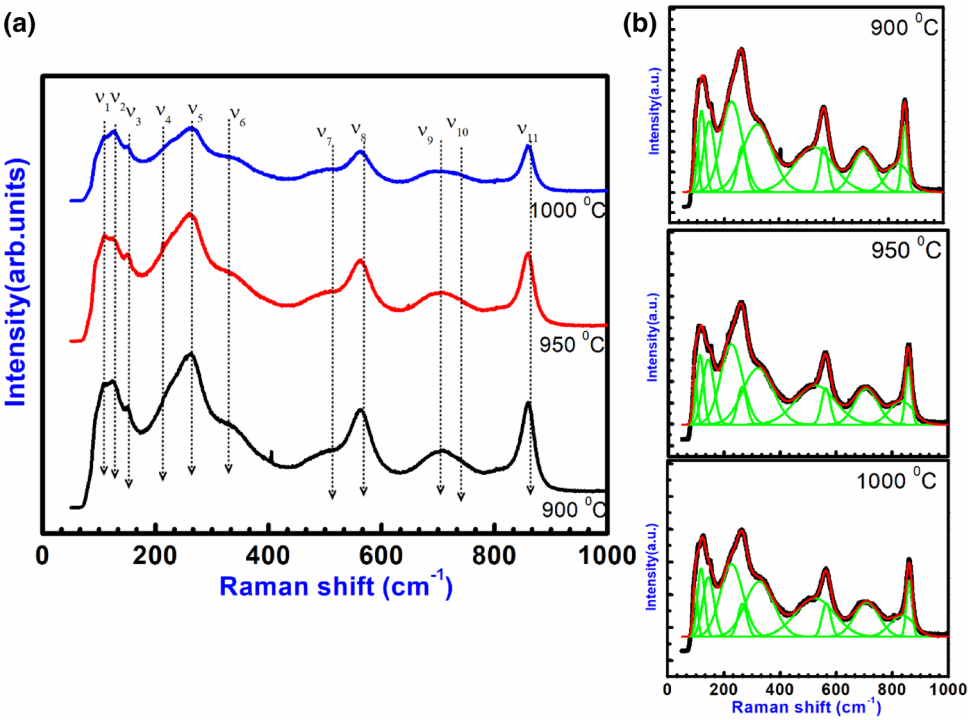

Fig. 4 **a** Raman Spectroscopic studies of $Bi_{4.0}Nd_{1.0}(Ti_3Fe)O_{15}$ sintered at various temperatures and **b** deconvoluted Raman spectra for the $Bi_{4.0}Nd_{1.0}(Ti_3Fe)O_{15}$ sintered at 900, 950 and 1000 °C

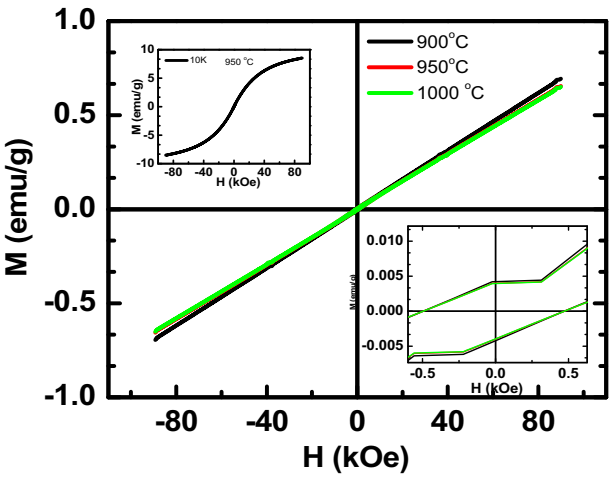

Fig. 5 Depiction of magnetization (M) vs magnetic field (H) hysteresis studies of $Bi_{4.0}Nd_{1.0}(Ti_3Fe)O_{15}$ ceramic sintered at 900 °C, 950 °C, and 1000 °C temperatures, respectively

currents are may be due to the presence of oxygen vacancies, defects, mixed-valence states of Fe- ions. The remanent polarization (P_r) and coercive fields (E_c) under the applied fields are shown in Fig. 6d. The observed P_r and E_c values are found to be maximum for the sample BNFT-950 compared to the other two samples. The improved ferroelectricity in it could be due to the maximum distortion of the lattice which can be reflected in terms of shift of XRD peaks toward a higher 2θ angle side and from the Raman spectra for BNFT-950 sample. The increase in 2θ indicates a decrease in the volume of the unit cell. The decrease in unit cell volume leads to the distortions in the oxygen octahedral and off-centering of cations and hence the improved ferroelectric properties of the sample. Further, for BNFT-1000 sample, the increase in sintering temperature would increase Bi- vacancies due to its volatile nature [34] which in turn increases the oxygen vacancies and hence, the deterioration of ferroelectric behavior in the BNFT-1000 sample.

3.6 Dielectric and impedance studies

The temperature variation of dielectric constant (ε_r) and loss tangent (Tanδ) at different frequencies are shown in Fig. 7 for the BNFT-950 sample. The dielectric constant increases steadily up to a certain temperature around 400 K and beyond this temperature, and the ε_r shows a broad anomaly around 650 K for all the frequencies as shown in Fig. 7a. A small change in the peak position of ε_r with frequency is observed, that is a typical characteristic of the relaxor behavior of BNFT samples. The dielectric loss data show relaxations between the temperature of 500–600 K as shown in the inset of Fig. 6b. The plot of dielectric relaxation temperature and frequency is

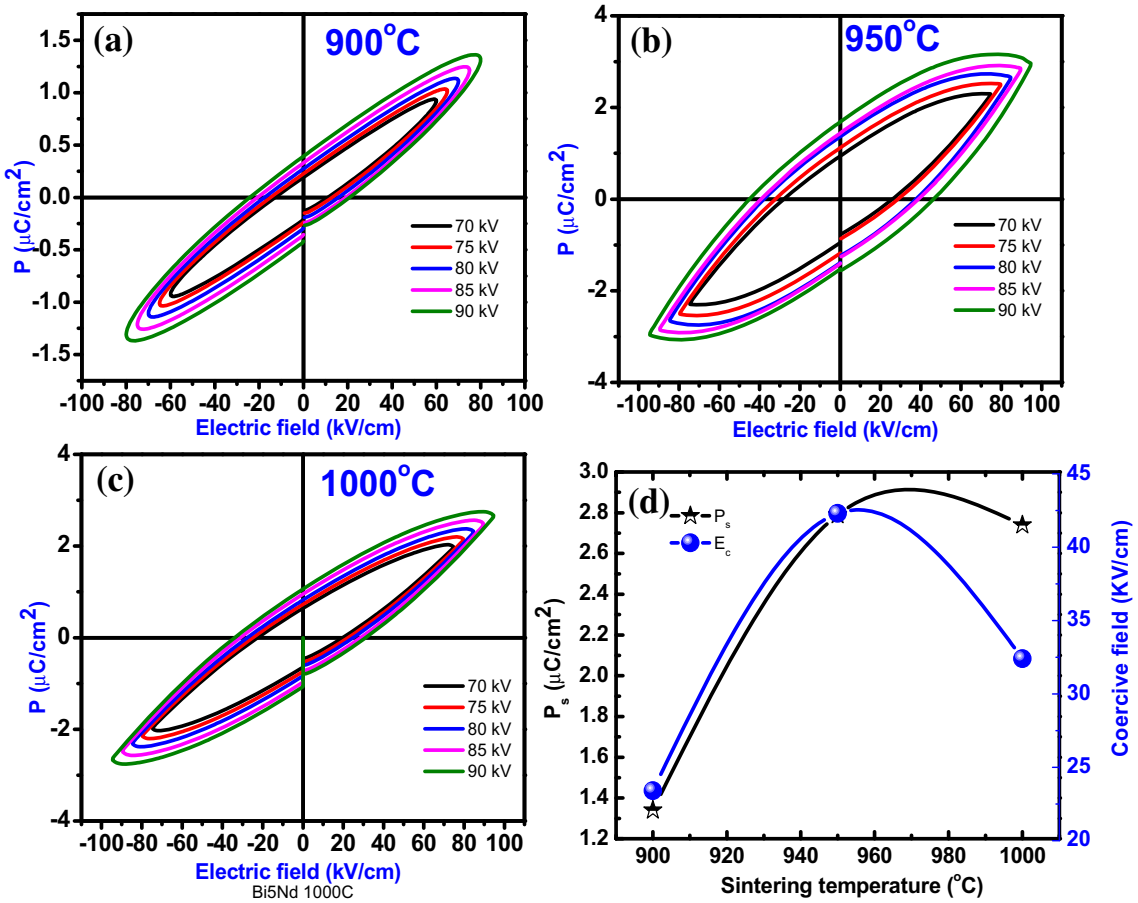

Fig. 6 Illustration of polarisation (P) vs electric field (E) hysteresis characteristics of $Bi_{4.0}Nd_{1.0}(Ti_3Fe)\ O_{15}$ ceramic sintered at temperatures **a** 900 °C **b** 950 °C **c** 1000 °C, respectively, and **d** comparison of coercive field (Ec) $Bi_{4.0}Nd_{1.0}(Ti_3Fe)\ O_{15}$ ceramic sintered at three various mentioned temperatures

observed to obey Arrhenius law $f = f_0 \exp\left(-\frac{E}{k_B T}\right)$. The activation energy E is estimated to be 0.59 eV by plotting log$f$ vs $1000/T$.

The frequency variation of dielectric constant and loss tangent Tanδ is shown in Fig. 8. The dielectric constant is high at low frequency and decreases with the increase in frequency. The high dielectric constant at low frequency is anticipated contributions from various types of polarizations such as space-charge, dipolar, ionic, and electronic polarization. As the frequency increases, the decrease in dielectric constant is due to the drop in contribution from space-charge polarization followed by the other contributions [35, 36]. The dielectric constant becomes constant at higher frequencies as the contribution is mainly due to electronic polarization only. The frequency-dependent dielectric loss data show dielectric relaxations in the low-frequency region. The relaxation peaks shift to a higher frequency side with the increase in temperature indicating a thermally activated relaxation process. The frequency (f_m) where the dielectric loss is maximum is plotted with respect to the temperature (log$f_m$vs $1000/T$) as shown in the inset of Fig. 8d. The linear fit of log$f_m$vs $1000/T$ is used to determine the activation energy (E_g). The obtained E_g value is 0.42 eV indicates that the relaxation is due to the short-range movements of oxygen vacancies [37, 38].

The frequency variation of real and imaginary parts of electric modulus is shown in Fig. 8b, the real part of electric modulus (M') increases with the increase in frequency, and then it becomes saturates at high frequencies. The M'' shows a maximum value at a particular frequency (M''_{max}) for a given temperature. The charge carriers perform long-range

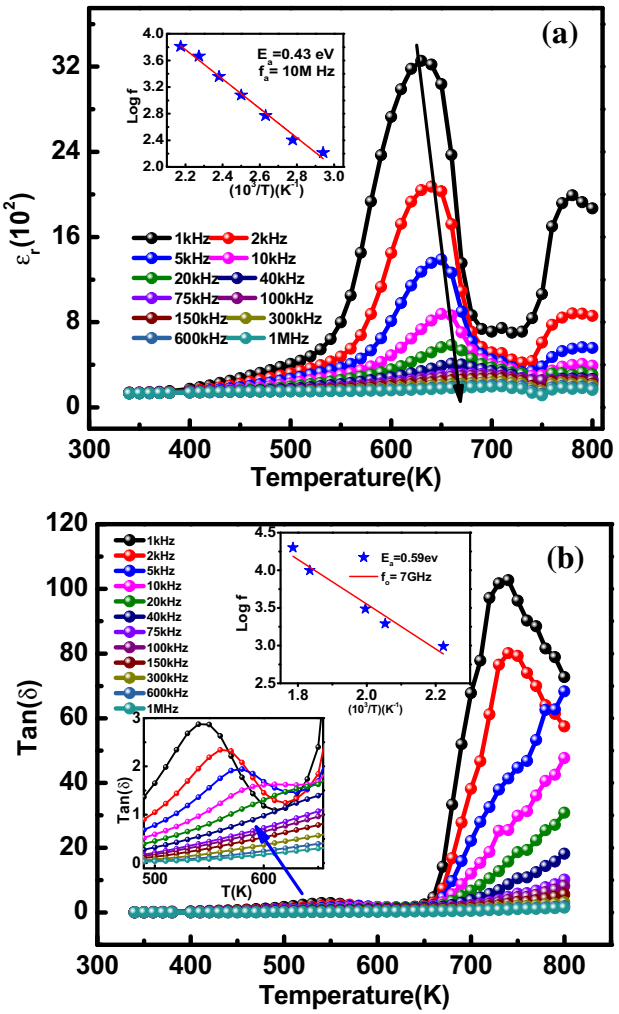

Fig. 7 Variation of **a** dielectric constant (ε') **b** dielectric loss tangent, Tanδ as a function of temperature for 950 °C sintered samples

hopping from one site to another site for the frequencies below f_{max}, whereas short-range hopping of charged particles is performed for frequencies above f_{max} [39]. The imaginary part of electric modulus (M'') shows relaxations which shifts to a higher frequency side with the increase in temperature as shown in Fig. 8(b). The variation of the frequency corresponding to the maximum value of M'' and temperature is following Arrhenius law $f = f_0 \exp\left(-\frac{E}{k_B T}\right)$. The activation energy E is estimated by plotting log$f$ vs 1000/T. The value of E is found to be 0.59 eV. Figure 8c shows the temperature variation of the real part of the electric modulus (M').

4 Conclusions

The four-layered $Bi_4NdTi_3FeO_{15}$ Aurivillius multiferroic ceramic was prepared via solid-state reaction at different sintering temperatures 900 °C, 950 °C, and 1000 °C. The samples exhibited an orthorhombic structure with $A2_1am$ space group as is evidenced by Rietveld refined room-temperature X-ray diffraction and Raman studies. The presence of a multiferroic character in Aurivillius ceramics either in three-layered BIT or four-layered BFTO structure not only due to the presence of B-site dopant with large magnetically active ions (Fe^{3+}) but also dopant of 4f (Nd, Sm, Gd) ion at A-site. In particular, the four-layered BFTO Aurivillius ceramics exhibit robust magnetic ordering owing to the low concentration of Fe^{3+} ions and their random occupancy at B-sites in octahedral positions. Therefore, the low concentration of Fe^{3+} leads to less probability of long-range ordering of the iron spins in BFTO that makes the ferromagnetic exchange interaction practically impossible to be achieved at room temperature. Henceforth, we noticed a weak ferromagnetic property in Nd-doped BNFT ceramics at room temperature. Till there is a debate on, the formation of magnetic property in layered Aurivillius not be the intrinsic, due to the possible formation of magnetically-active secondary phases.

The proper sintering temperature might induces a strong density in grains growth mechanism and that leads a strong ferroelectric character. Therefore, we noticed improper ferroelectric loops at room temperature @ 950 °C sintered ceramics, indicate stabilize the ferroelectric character in measured ceramics. Thus, these experimental outcomes conclude the presence of a multiferroic character in Nd-doped BFTO ceramics at room temperature. Optimum sintered sample @ 950 °C detailed dielectric relaxation and modulus spectroscopy study were ascribed to short-range movements of oxygen vacancies. Henceforth, the study of Aurivillius rare-earth-doped 4-layer multiferroic materials can be useful for wide variety room temperature multiferroic applications.

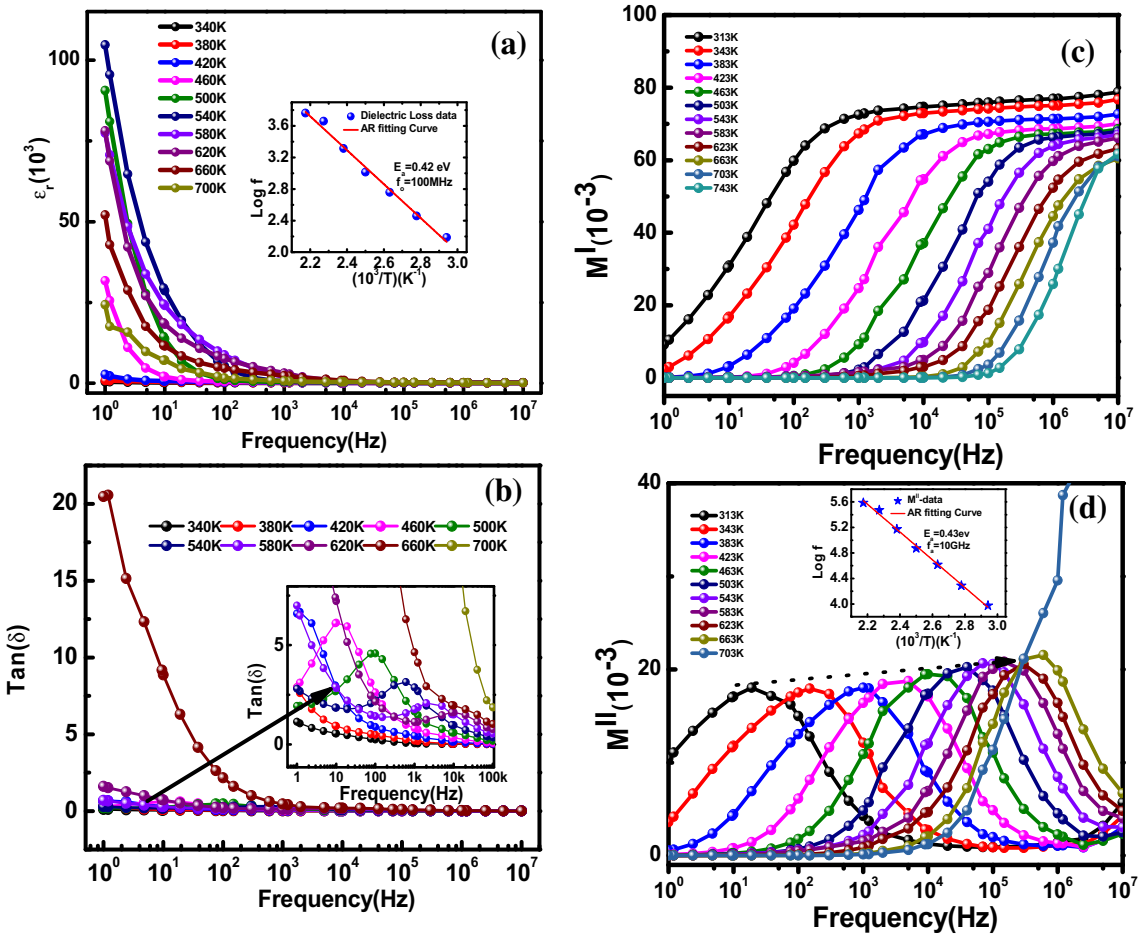

Fig. 8 Variation of **a** dielectric constant (ε') **b** Tanδ **c** real part of modulus (M') and Imaginary part of Modulus (M'') as a function frequency with variation in temperature for $Bi_{4.0}Nd_{1.0}(Ti_3Fe)\ O_{15}$ Ceramics sintered at 950 °C

Acknowledgement

The authors would like to thank UGC-DAE Consortium, Mumbai Centre, India for providing experimental facilities. Dr. Tirupathi Patri is greatly thankful to UGC-DAE Consortium, Mumbai Centre, India for financial support under UGC-DAE, CRS-M-261-Sponsored Project Scheme.

Declarations

Conflict of interest All authors declare that they have no conflict of interest.

References

1. W. Eerenstein, N.D. Mathur, J.F. Scott, Nature **442**, 759 (2006)
2. F. Kubel, H. Schmid, Ferroelectrics **129**, 101 (1992)
3. D. Zhang, L. Feng, W. Huang, W. Zhao, Z. Chen, X. Li, J. Appl. Phys. **120**, 154105 (2016)
4. P. Tirupathi, H. S. K. Reddy, P. D. Babu, in *AIP Conf. Proc.* (AIP Publishing LLC, 2018), p. 40014.
5. B.H. Park, S.J. Hyun, S.D. Bu, T.W. Noh, J. Lee, H.-D. Kim, T.H. Kim, W. Jo, Appl. Phys. Lett. **74**, 1907 (1999)
6. B. Aurivillius, Ark. Kemi **1**, 463 (1949)
7. E.C. Subbarao, J. Am. Ceram. Soc. **45**, 166 (1962)
8. J. Yang, L.H. Yin, Z. Liu, X.B. Zhu, W.H. Song, J.M. Dai, Z.R. Yang, Y.P. Sun, Appl. Phys. Lett. **101**, 12402 (2012)
9. S.B. Desu, P.C. Joshi, X. Zhang, S.O. Ryu, Appl. Phys. Lett. **71**, 1041 (1997)
10. H.N. Lee, D. Hesse, N. Zakharov, U. Gösele, Science (80-) **296**, 2006 (2002)
11. Z. Zhou, X. Dong, H. Chen, H. Yan, J. Am. Ceram. Soc. **89**, 1756 (2006)

12. X.W. Dong, K.F. Wang, J.G. Wan, J.S. Zhu, J.-M. Liu, J. Appl. Phys. **103**, 94101 (2008)
13. T. Patri, R. Patangi, K.R. Kandula, K. Banerjee, S. Asthana, P.D. Babu, J. Mater. Sci. Mater. Electron. **31**, 874 (2020)
14. A. Srinivas, S.V. Suryanarayana, G.S. Kumar, M.M. Kumar, J. Phys. Condens. Matter **11**, 3335 (1999)
15. X. Mao, W. Wang, X. Chen, Y. Lu, Appl. Phys. Lett. **95**, 82901 (2009)
16. J. Xiao, H. Zhang, Y. Xue, Z. Lu, X. Chen, P. Su, F. Yang, X. Zeng, Ceram. Int. **41**, 1087 (2015)
17. J. Liu, W. Bai, J. Yang, W. Xu, Y. Zhang, T. Lin, X. Meng, C.-G. Duan, X. Tang, J. Chu, J. Appl. Phys. **114**, 234101 (2013)
18. T. Patri, J. Praveen Kumar,A. Ghosh. and P. D. Babu., J. Appl. Phys. (2020) (Accepted Manuscript).
19. P. Mandal, M.J. Pitcher, J. Alaria, H. Niu, P. Borisov, P. Stamenov, J.B. Claridge, M.J. Rosseinsky, Nature **525**, 363 (2015)
20. A.Y. Birenbaum, C. Ederer, Phys. Rev. B **90**, 214109 (2014)
21. H. Zhao, H. Kimura, Z. Cheng, M. Osada, J. Wang, X. Wang, S. Dou, Y. Liu, J. Yu, T. Matsumoto, Sci. Rep. **4**, 1 (2014)
22. P. Tirupathi, S.K. Mandal, A. Chandra, J. Appl. Phys. **116**, 244105 (2014)
23. J.M. Herbert, *Ferroelectric Transducers and Sensors* (CRC Press, London, 1982).
24. J. Ilczuk, D. Machura, J. Rymarczyk, Mol. Quantum Acoust. **28**, 107 (2007)
25. J.A. Horn, S.C. Zhang, U. Selvaraj, G.L. Messing, S. Trolier-McKinstry, J. Am. Ceram. Soc. **82**, 921 (1999)
26. X. Zuo, M. Zhang, E. He, B. Guan, Y. Qin, J. Yang, X. Zhu, J. Dai, J. Alloys Compd. **726**, 1040 (2017)
27. J. Hou, Y. Qu, R. Vaish, K.B.R. Varma, D. Krsmanovic, R.V. Kumar, J. Am. Ceram. Soc. **93**, 1414 (2010)
28. T. Patri, J. Ponnaiah, P. Kutty, A. Ghosh, Ceram. Int. **42**, 13834 (2016)
29. J. Liu, G. Zou, Y. Jin, J. Phys. Chem. Solids **57**, 1653 (1996)
30. J. Zhu, X.-B. Chen, J. He, J.-C. Shen, Phys. Lett. A **362**, 471 (2007)
31. C.M. Raghavan, J.W. Kim, J.-W. Kim, S.S. Kim, Ceram. Int. **40**, 10649 (2014)
32. G. Chen, W. Bai, L. Sun, J. Wu, Q. Ren, W. Xu, J. Yang, X. Meng, X. Tang, C.-G. Duan, J. Appl. Phys. **113**, 34901 (2013)
33. F. Gao, C. Cai, Y. Wang, S. Dong, X.Y. Qiu, G.L. Yuan, Z.G. Liu, J.-M. Liu, J. Appl. Phys. **99**, 94105 (2006)
34. T. Durga Rao, B. Sattibabu, S. Asthana, Phys. Status Solidi **256**, 1900097 (2019)
35. Y. Shi, Y. Pu, J. Li, R. Shi, W. Wang, Q. Zhang, L. Guo, Ceram. Int. **45**, 9283 (2019)
36. X. Zhu, J. Yang, D. Dastan, H. Garmestani, R. Fan, Z. Shi, Compos. Part A Appl. Sci. Manuf. **125**, 105521 (2019)
37. T.D. Rao, T. Karthik, A. Srinivas, S. Asthana, Solid State Commun. **152**, 2071 (2012)
38. P. Tirupathi, P. Justin, K. Prabahar, M. Poster, J. Alloys Compd. **731**, 411 (2018)
39. T. Durga Rao, R. Ranjith, S. Asthana, J. Appl. Phys. **115**, 124110 (2014)